

Shape Comparison between 0.4–2.0 and 20–60 μm Cement Particles

Lorenz Holzer

Empa Materials Science and Technology, 3D-Mat, CH-8600 Dübendorf, Switzerland

Robert J. Flatt

Sika Technology AG, Corporate Research and Analytic, CH-8048 Zürich, Switzerland

Sinan T. Erdoğan

Department of Civil Engineering, Middle East Technical University, Ankara, Turkey

Jeffrey W. Bullard and Edward J. Garboczi[†]

Inorganic Materials Group, National Institute of Standards and Technology, Gaithersburg, Maryland 20899-8615

Portland cement powder, ground from much larger clinker particles, has a particle size distribution from about 0.1 to 100 μm . An important question is then: does particle shape depend on particle size? For the same cement, X-ray computed tomography has been used to examine the 3-D shape of particles in the 20–60 μm sieve range, and focused ion beam nanotomography has been used to examine the 3-D shape of cement particles found in the 0.4–2.0 μm sieve range. By comparing various kinds of computed particle shape data for each size class, the conclusion is made that, within experimental uncertainty, both size classes are prolate, but the smaller size class particles, 0.4–2.0 μm , tend to be somewhat more prolate than the 20–60 μm size class. The practical effect of this shape difference on the set-point was assessed using the Virtual Cement and Concrete Testing Laboratory to simulate the hydration of five cement powders. Results indicate that nonspherical aspect ratio is more important in determining the set-point than are the actual shape details.

I. Introduction

PORTLAND cement powder, ground from much larger clinker particles, has a wide particle size distribution (PSD), from about 0.1 to 100 μm . An important question is then: does particle shape depend on particle size? When one is modeling cement particles and their transformation via hydration into a three-dimensional (3-D) microstructure, one needs to know if any shape dependence on size needs to be addressed as one builds 3-D models.

Many properties of composite materials composed of a matrix with particulate inclusions depend, with different degrees of sensitivity depending on the property, on the 3-D shape of the inclusions.^{1–4} Concrete (cement+water+sand+gravel) shows this same character at different length scales. At the millimeter length scale, there is a mortar (cement+water+sand) matrix and coarse aggregate inclusions. The shape of coarse aggregates is treated in the ASTM standards.⁵ At the micrometer scale, the cement paste (cement+water) matrix of concrete is a composite composed of cement particles in a matrix—water—which then dissolve and react to form new phases. Because cement particles

dissolve and react, losing shape information at later ages, the effect of cement particle shape is most clearly seen at early ages, where reaction can be controlled by nucleation on cement particle surfaces and where setting is controlled by percolation of a solid network that bridges cement particles. Both specific surface area and percolation questions are known to be dependent on particle shape. A model investigation of the effect of particle shape on early age hydration has been carried out, and an effect was clearly seen—according to the model, the nonspherical particles had more hydration at the same early age than did the spherical particles.^{6,7} Because a sphere has the minimal surface area for a given volume,⁴ any change of cement particle shape away from spherical will increase the surface area to volume ratio and thus the early age reaction kinetics. The effect of cement particle shape on early age concrete rheology may also be important.⁸

However, there are no standard shape tests for cement particles. Particle size techniques like laser diffraction interpret each size class as spherical particles. While it is known that nonspherical shape can bias the sizes found with this technique,⁹ one cannot, at this point, get quantitative information about shape from this technique.^{10–13}

A recent study¹⁴ has investigated particle shape differences between different cements that were ground similarly in a ball mill. This study demonstrated that there is a dependence of particle shape on cement particle mineralogy, when comparing particles of the same size as judged by identical sieving. One could imagine that there might also be a dependence of particle shape on particle size, since, for example, the smallest particles are simply small chips off larger particles, so they might tend to have a more angular shape than larger particles that have been rounded off by losing such small chips. As the smaller particles tend to hydrate faster than larger particles, because of their larger surface area to volume ratio, any shape difference from the larger particles could interact with this size difference, further influencing early age reaction kinetics.

To investigate particle shape dependence on particle size requires that one be able to quantitatively evaluate 3-D particle shape over a wide range of size. The shape information available from X-ray computed microtomography (CT)¹⁴ does not cover a sufficiently wide size range, since a particle must be at least 10 voxels wide to get reasonably accurate shape information, and the smallest voxel size commonly available, on machines like the synchrotron at Brookhaven National Laboratory¹⁴ or ESRF in France,¹⁵ is around 1 μm or slightly less. That limits the smallest cement particle to be about 10 μm wide, and cement particles are usually <60 μm . Recent dual focused ion beam work^{16–18} has

G. Scherer—contributing editor

Manuscript No. 26921. Received October 5, 2009; approved January 6, 2009.

[†]Author to whom correspondence should be addressed. e-mail: edward.garboczi@nist.gov

enabled 3-D images to be made of cement particles in the size range of 0.4–2.0 μm . Again, this is not a wide enough size range for the question of shape dependence on size to be determined. However, by combining these two techniques, used on the same cement ground in a ball mill, one can compare particles whose size differs by a factor of 10–100, probably a large enough size difference to see any effect of particle size on particle shape. Note that particles from 2.0 to 20 μm in size are neglected in this study, as no experimental technique that could access 3-D particle shape in this size range was available to us at the time of this study. It is possible that this cement, if prepared in a roller mill instead of a ball mill, might give somewhat different shape results, but investigation of this is beyond the scope of this paper.

In this paper, spherical harmonic techniques^{19,20} are used to analyze each image data set and compute many shape-related parameters. The practical effect of this shape difference on set point is approximately assessed using the Virtual Cement and Concrete Testing Laboratory (VCCTL)^{21,22} to compute the hydration of five cement powders, all with the same chemistry, and having a variety of shapes: spheres, rectangular boxes, and real shapes from the two size classes studied. Further understanding of particle size versus shape relations for cements will give insight into experiments where particle size matters, and will aid in the development of cement hydration models that take particle size and shape directly into account.^{23,24}

II. Experimental Procedure

(1) X-Ray CT

In CT, X-rays penetrate a 3-D sample at many different angles and the absorption is measured. A computer-based reconstruction technique then makes gray level images, where each image is a slice of the sample and the contrast in gray levels is caused by the different X-ray absorption properties of the materials in the sample, which usually are caused by density differences.²⁵ A cubic voxel 1 μm in dimension was used for the CT results in this paper.

The resulting 3-D image, made by stacking the many 2-D images of the sample, is a gray-scale image that needs to be segmented to produce the final binary image containing the aggregates. In this paper, the 3-D images considered are of a dispersion of cement particles in epoxy. In the segmented 3-D image, details below the voxel size have been lost, and it is possible that the volume of the particles in the image could be a little smaller or a little larger than reality, due to the choice of threshold used in the segmentation process, which was chosen so that the binary image closely matched the original gray scale image. Each sample in general had a different threshold, which depends on sample preparation, cement composition, and X-ray CT equipment settings. The gray scale also differed between individual cement particles, due also to mineralogical differences between particles. These interparticle differences were lost when preparing segmented particle-epoxy binary images, since only overall particle shape was studied, not particle interior details. For larger particles whose volumes could be easily experimentally measured, the processed CT data did give an accurate value of particle volume.²⁰

(2) Focused Ion Beam Nanotomography (FIB-NT)

FIB-NT is a high-resolution 3D-imaging technique that is based on an automated serial section procedure.¹⁸ A gallium ion beam is used to erode layers as thin as 20 nm. The electron beam is then used to acquire images from freshly exposed planes in a scanning electron microscopy (SEM) mode. In this way, a stack of images can be produced in a repetitive procedure. Since the distance between the single layers is in the same range as the pixel resolution of the images, the entire stack of images becomes a voxel-based data volume.

For all serial sectioning methods, the precision of the milling procedure is the main factor that limits the overall resolution. In FIB-NT, the resolution in the z -direction (i.e., the resolution

perpendicular to the SEM imaging plane) is dependent on both the interaction depths of the gallium ions used during FIB milling and of the electrons used during SEM imaging. As the direction of ion-milling is parallel to the x - y plane (in-plane milling), this geometry significantly reduces the depth penetration of the gallium ions. Therefore, the amorphization of the surface layer, which is the main milling artifact, is limited to a depth of only a few nanometers. In addition, this amorphization does not significantly destroy the initial material-density contrast in the sample and hence the material microstructure can still be resolved by SEM/backscattered electron (BSE) imaging. More critical for the resolution in the z -direction is the depth penetration of the electrons during SEM/BSE imaging. The effect of electron depth penetration on resolution is difficult to quantify as it is dependent on several parameters such as the acceleration voltage, the material density, and mean atomic number. Nevertheless, tests with spherical SiO_2 nanoparticles confirm that particle shapes with curvature radii in the 100 nm-range can be reliably resolved when FIB-NT is performed in combination with low energy electron SEM-imaging.¹⁸

Finite size effects are a major problem for inhomogeneous samples, as the imaging window (i.e., the analyzed volume) is strongly limited at high magnifications. Thus, magnification has to be adapted according to the object size to include a statistically meaningful sampling from the population of particles. In a previous study^{16,17} of the same cement used in this paper, different grain size fractions were analyzed (d_{50} ranging from 2 to 9 μm) at different magnifications (voxel resolution ranging from 32 to 74 nm). For quantitative analysis of the FIB-NT data, special procedures have been developed for accurate object recognition (separation of particles in densely packed microstructures) and for stereological correction of truncation effects at the volume boundaries.¹⁷

(3) Spherical Harmonics

3-D voxel data generated in any fashion (e.g., X-ray CT,¹⁹ laser range-finding or Ladar²⁶) can be used to generate spherical harmonic functions,¹⁹ which can then be used to create a smooth approximation to the function $r(\theta, \phi)$, which is the distance from the center of volume to the surface in the direction given by the spherical polar angles (θ, ϕ) . Using this function, one can compute any geometric quantity of the particle like volume, surface area, or moment of inertia.^{19,20,27,28} One caveat is that the particle must be star shaped.¹⁹

The spherical harmonic mathematical analysis relies on Eq. (1), which states that any sufficiently smooth function $r(\theta, \phi)$, where θ and ϕ are the azimuthal and polar angles of 3-D spherical coordinates, can be written as a series of spherical harmonic functions, where the Y_{nm} are the complex spherical harmonic functions and the a_{nm} are complex coefficients²⁹:

$$r(\theta, \phi) = \sum_{n=0}^N \sum_{m=-n}^n a_{nm} Y_{nm}(\theta, \phi) \quad (1)$$

Strictly speaking, the series in Eq. (1) becomes exact only as $N \rightarrow \infty$. However, like 2-D Fourier series, a finite value of N is usually found to give an adequate approximation of a given function, within some specified uncertainty limit.

Using a numerically determined $r(\theta, \phi)$ function from a 3-D voxel image of a single particle, derived from the CT images or from the FIB-NT images, one can accurately determine the first $N = 20$ or so coefficients in Eq. (1), which are usually enough to satisfactorily represent the particle. In the cases studied in this paper, the values of accurate N range from $N = 16$ to 26, with most cases having a value of N of about 20.

(4) Materials and Sample Preparation

FIB-NT analyses were performed with seven different grain size ranges of an ordinary portland cement (OPC CEMI 32.5R,

Lafarge Cement U.K., Oxon, U.K.).[‡] Number 1 contained the smallest particles and number 7 contained the largest particles. These grain size fractions were separated from the dry cement powder by air classification (Alpine MRZ2, Hosokawa, Alpine AG, Augsburg, Germany). For each fraction, 10%, 50%, and 90% fractiles were determined by laser diffraction (Malvern Zetasizer 4, Malvern, Worcestershire, U.K.), using 5-min ultrasonic treatment in ethanol. For the seven size ranges, the 90% fractiles (90% by mass of the particles were smaller than this size) were: 1–2.4, 2–4.6, 3–8.8, 4–15.0, 5–24.0, 6–34.0, and 7–45.5 μm .¹⁶

The samples for FIB-NT analysis were prepared by compacting the dry powders (size fractions number 1 to number 5) at moderate pressures in a small cylinder (5 mm diameter, 10 mm height) and then impregnating the samples with epoxy resin. The two largest size fractions, number 6 and number 7, were not used in the FIB-NT measurements. The subsequent grinding and polishing steps were identical to those used when preparing scanning electron microscope samples.

Details about the CT sample preparation are given in Erdogan *et al.*⁹. The cement from the largest size range, number 7, was mixed with epoxy, after having first been sieved to remove particles $<20 \mu\text{m}$ in size, as determined by the sieve opening. Smaller particles, which cannot be adequately resolved (those smaller than about five to 10 times the voxel size), complicate image processing because they appear blurred. It was found that slow mixing resulted in fewer air bubbles, and placing the samples in a vacuum for 2–3 min eliminated any remaining large bubbles. The epoxy mixture was inserted into small plastic cylinders of diameter 3–5 mm. The amount of particles in the mixture should not exceed a volume fraction of about 15%. Higher contents caused problems with image processing (e.g., too many touching particles) and a sufficient number of particles of a certain type can be characterized with one scan at this concentration. The heights of the specimens were 20–60 mm; however, this value could be much lower as the part of the specimen scanned was often $<2 \text{ mm}$ high.

III. Size and Shape Parameters

The size of a spherical particle is precisely determined by one number, its diameter, and of course its shape is known precisely. Other known-shape particles like ellipsoids and rectangular parallelepipeds are similar but require three numbers to define the size and shape. For an irregular particle, like all cement particles, there is no one number or even a small set of numbers that can precisely quantify the size and shape. There are, however, several ways to approximately assign a single “size” number to an irregular particle. One way is to compute the diameter of a sphere that has a volume equal to that of the irregular particle. In this paper, this diameter is termed the volume equivalent spherical diameter (VESD), and is used as a convenient but nonrigorous way to classify particles by size. Another way is to use a sieve analysis, and use the range between sieves to define the size. Sieve sizes are often thought of as equivalent spherical diameters. The two VESD ranges that we are considering are 0.4–2.0 and 20–60 μm .

One can try to define three numbers to characterize an irregular particle: the length, the width, and the thickness.^{5,20} The length (L) is defined as the largest straight-line surface point-to-surface point distance on the particle. The width (W) is defined similarly, except that it must be perpendicular to the length. The thickness (T) is also defined similarly, except that it must be perpendicular to both the length and the width. L , W , and T define some kind of equivalent rectangular parallelepiped for the irregular particle, or they could be interpreted as the axis lengths of a tri-axial ellipsoid. If $L = W = T$, then the particle is similar in some way to a sphere or a cube, i.e., it is equiaxed. By defini-

tion, $T < W < L$. If W is significantly larger than T , and $L \approx W$, then the particle tends to be oblate. If $W \approx T$ but L is significantly larger than W , then the particle is somewhat prolate. In this paper, the computed values of L and W are normalized by the value of T , forming two independent, dimensionless ratios for each particle: $\mathcal{L} \equiv L/T$ and $\mathcal{W} \equiv W/T$, called the normalized length and width.

IV. Results

There were 1665 particles reconstructed and analyzed from the FIB-NT results, and 749 particles taken from the CT results, both taken from the same cement but from different size classes. One simple comparison to make between the two sets of particles is between the average normalized lengths and widths ($\langle Q \rangle = \text{average of } Q$). A range in length and width was expected for each particle set, so that the standard deviation for each average just shows the kind of variability each particle set showed. For the FIB-NT particles, $\langle \mathcal{L} \rangle = 2.06 \pm 0.61$, while for CT the average length was 20% smaller, $\langle \mathcal{L} \rangle = 1.71 \pm 0.35$. The standard deviation divided by the average is 0.3 for the FIB-NT particles, while this ratio is 0.2 for the CT particles, indicating a narrower distribution for the CT particles. For the widths, FIB-NT gave $\langle \mathcal{W} \rangle = 1.42 \pm 0.27$ while CT gave $\langle \mathcal{W} \rangle = 1.35 \pm 0.23$. These results were much closer, only a difference of 5% and with nearly identical ratios of standard deviation to average.

Additional insight can be gained by computing and comparing the distribution functions for the normalized lengths and widths. The normalized distribution function for a individual particle parameter P , $f(P)$, is defined such that $f(P) dP$ is equal to the number fraction of particles whose value of P lies between P and $P + dP$. The number fraction is defined as the fraction of the total particle number, and the integral of $f(P)$ over the limits of P is equal to unity.

Figure 1 shows the distribution functions for \mathcal{L} for both sets of particles. Clearly, the distribution function for the smaller FIB-NT particles is wider and peaked at a larger length value, consistent with the average and standard deviation of the particle lengths. Figure 2 shows the normalized distribution function for the widths. Notice that the distributions seem almost identical. Each curve is somewhat “noisy,” due to the fairly small number of particles used to compute the curves. A larger number of particles would reduce this noise and give a smoother curve.

If the assumption is made that, for the dimensionless width and length, the distributions have the same functional form, one can use the Student t -test³⁰ to show that both of the parameters for the dimensionless width and length distributions, mean

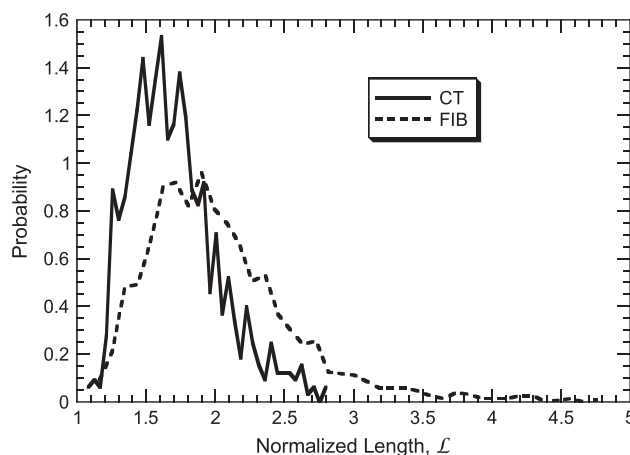


Fig. 1. The length distribution for the two particle size classes, in terms of number fraction. The two particle size classes are referred to by the technique that was used to image them. CT, computed tomography; FIB, focused ion beam.

[‡]Certain commercial equipment and/or materials are identified in this report in order to adequately specify the experimental procedure. In no case does such identification imply recommendation or endorsement by the National Institute of Standards and Technology, nor does it imply that the equipment and/or materials used are necessarily the best available for the purpose.

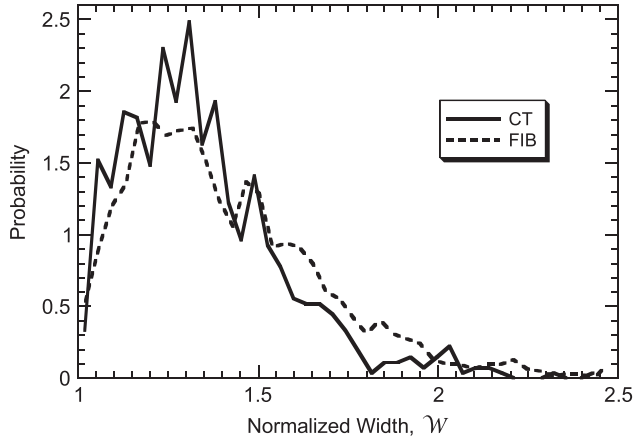


Fig. 2. The width distribution for the two particle size classes, in terms of number fraction. The two particle size classes are referred to by the technique that was used to image them. CT, computed tomography; FIB, focused ion beam.

and standard deviation (square root of the variance), have <1% probability of being the same, so that statistically, these parameters are probably different for the CT and FIB-NT sets of particles.

A more qualitative look at the shape differences between the two particle size classes expression “more prolate” can be obtained by considering Figs. 3 and 4, which show the $\mathcal{R} = \langle L/W \rangle$ values for each particle in each size set. The FIB-NT average value of L/W was $\mathcal{R} = 1.46 \pm 0.35$, while the CT average L/W value was $\mathcal{R} = 1.27 \pm 0.18$, indicating that the FIB-NT particles are more “prolate” than the X-ray CT particles.

Figures 5 and 6 are similar to Figs. 3 and 4, but show, for each particle, the ratio of the maximum principal moment of inertia to the minimum principal moment of inertia, I_{\max}/I_{\min} . The moment of inertia tensor is defined for a particle in any classical mechanics textbook,³¹ and the details of how to compute this for particles represented by a spherical harmonic series have been given.¹⁹ The principal moments of inertia are defined to be the diagonal elements of the tensor after it has been diagonalized (I_1, I_2, I_3). The ratio of the maximum (I_{\max}) to the minimum (I_{\min}) values has been used previously as a measure of particle anisotropy.¹⁷

It appears from Figs. 5 and 6 that the moment of inertia ratio shows a larger difference between the particles than does the length/width ratio in Figs. 3 and 4. Note that the average value of $I_{\max}/I_{\min} \equiv \mathcal{I}$ for the FIB-NT data is $\mathcal{I} = 2.27 = (1.51)^2$,

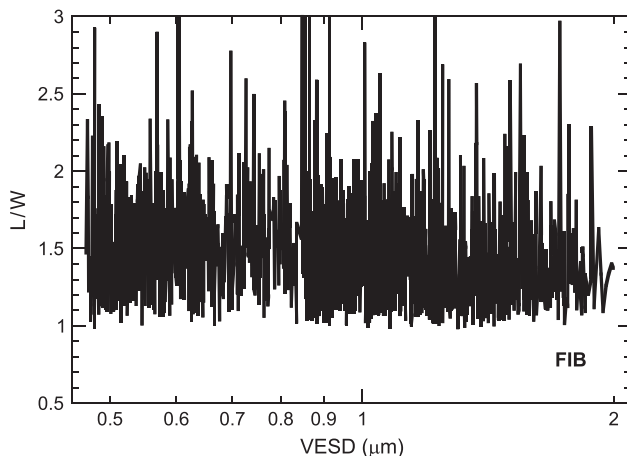


Fig. 3. Length to width ratio for particles with volume equivalent spherical diameter (VESD) between 0.4 and 2.0 μm (focused ion beam nanotomography [FIB-NT]), $\mathcal{R} = \langle L/W \rangle = 1.46 \pm 0.35$.

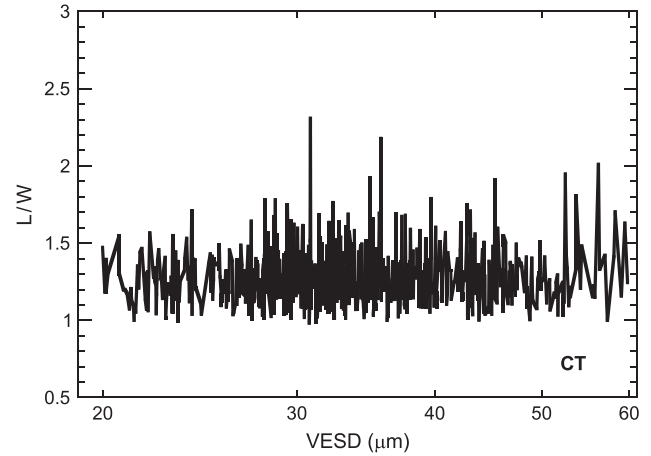


Fig. 4. Length to width ratio for particles with volume equivalent spherical diameter (VESD) between 20 and 60 μm (CT), $\mathcal{R} = \langle L/W \rangle = 1.27 \pm 0.18$. CT, computed tomography.

where $1.51 \cong 1.46 =$ the average value of L/W for this particle size range, and for the CT data, $\mathcal{I} = 1.795 = (1.34)^2$, where $1.34 \cong 1.27 =$ the average value of L/W for this data set. So for these random cement powder shapes, the relationship between \mathcal{I} and \mathcal{R} is roughly quadratic, i.e., $\mathcal{I} \approx \mathcal{R}^2$. This quadratic relationship has been found analytically for rectangular boxes and triaxial ellipsoids (see Appendix A). This approximately quadratic relationship between L/W and \mathcal{I} explains why Figs. 5 and 6 seem to indicate that the value of \mathcal{I} shows a more prolate character for the smaller particles, since \mathcal{I} is approximately a square of a number greater than one.

V. Model Hydration Comparison of Different Particle Shapes

One reason for studying how cement particle shape depends on cement particle size is to see how particle shape differences could affect hydration results. The smallest cement particles tend to hydrate more quickly than do the larger particles, because of their larger ratio of surface area to volume (S/V). As mentioned above, a previous study⁷ had explored the effect of particle shape on hydration and microstructural formation in cement paste using the National Institute of Standards and Technology (NIST) VCCTL^{21,22} hydration model, which is built upon a previous NIST model, CEMHYD3D.³² In this previous study,⁷ the range of the cement PSD used extended down to 1 μm . The

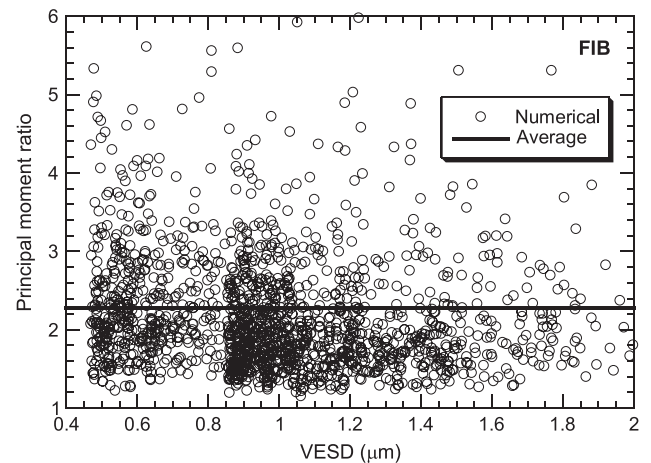


Fig. 5. Ratio maximum to minimum principal moment of inertia for particles with volume equivalent spherical diameter (VESD) between 0.4 and 2.0 μm (focused ion beam nanotomography [FIB-NT]), $\mathcal{I} = 2.27 \pm 1.3$.

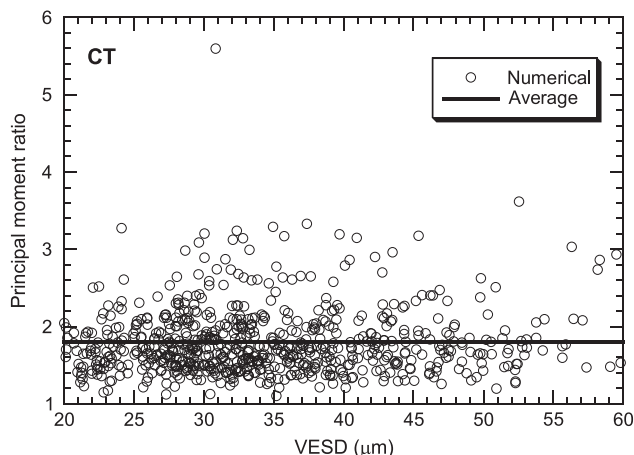


Fig. 6. Ratio of maximum to minimum principal moment of inertia for particles with volume equivalent spherical diameter (VESD) between 20 and 60 μm (computed tomography [CT]), $\mathcal{I} = 1.80 \pm 0.4$.

VCCTL hydration model is a 3-D digital model, with a resolution of 1 $\mu\text{m}/\text{voxel}$.³³ The smallest particles, say less than about 5 μm , did not have their shape faithfully represented, since it takes about five voxels to 10 voxels across a particle to represent the shape with acceptable accuracy.^{19,20,28} In fact, the 1 μm particles, which were the smallest particles included, were only one voxel in size and thus a perfect cube. There are certainly real particles with $L \approx W \approx T$, but in the VCCTL hydration module, there are a few percent by mass of these single voxel particles, which is larger than in reality. However, the comparison in Bullard and Garboczi⁷ was between spherical particles and real-shape particles, so a difference was still seen, because all the particles do start reacting at early-age, even though smaller particles, with their larger surface area to volume ratio, are consumed first.

For this paper, an accurate comparison of hydration behavior between the two particle shapes studied, FIB-NT and CT, was desired. However, this comparison was hindered by the fact that the two particle shape sets were at much different sizes and so would have different hydration behavior. Since the only interest was in the effect of particle shape differences on hydration behavior, model particles were prepared at equal volume and at sizes large enough so that the shape was faithfully reproduced in the digital image model. Systems of size 200^3 were employed to minimize finite size effects, and the set point was computed as the degree of hydration when the cement and any hydration products percolated through cement—C—S—H—cement contacts.³⁴ The effect of voxel resolution on set point was not explored, since particle shape was the focus, so all systems had the same resolution of 1 $\mu\text{m}/\text{voxel}$.³³ All results were averaged over five configurations for each shape set, and the standard deviation of the set point for each shape set was calculated based on these five independent results. A random arrangement/placement of cement particles was used, with no attempt made either to flocculate or disperse the particles.³²

The PSD used for all particle shapes was an artificial one, with no small particles and no particles larger than one eighth the size of the system, to avoid finite size effects.^{35,36} The PSD was based on five spheres, with diameters equal to 10, 14, 18, 22, and 24 μm , at a voxel size of 1 μm . The mass fractions of each size class were 0.12, 0.23, 0.3, 0.22, and 0.13, from small to large diameters.

Five different particle shapes were used: (1) spheres, (2) FIB-NT particle shapes, (3) rectangular boxes with similar L , W , and T statistics as the FIB-NT shapes, (4) X-ray CT particle shapes, and (5) rectangular boxes with similar L , W , and T statistics as the CT shapes. For the nonspherical particles, the exact same particle volumes were used, so that in all the systems simulated, there was exactly the same number of

Table I. Numerical Set Point Results for Hydration Simulations

Particles	α (0.4)	α (0.95)
Spheres	3.6 ± 0.1	6.1 ± 0.2
μCT	3.2 ± 0.1	5.0 ± 0.3
Equivalent box	3.2 ± 0.1	5.1 ± 0.2
FIB-nt	3.0 ± 0.1	4.8 ± 0.2
Equivalent box	3.1 ± 0.3	4.7 ± 0.3

The second column is the average degree of hydration at which 40% of the solids belonged to a percolated cluster. The third column indicates the average degree of hydration when 95% of the solids belonged to a percolated cluster. μCT , microcomputed tomography; FIB-NT, focused ion beam nanotomography.

particles, with exactly the same volumes, but with different shapes. The rectangular boxes were included to see which mattered more: the irregularity of the real shapes or the fact that they were angular and nonspherical. For the boxes based on the real particles, values of \mathcal{L} and \mathcal{W} were uniformly and randomly picked from the ranges $\mathcal{L} \pm \Delta$, $\mathcal{W} \pm \Delta$ where Δ is the appropriate standard deviation, and then the volume of the box was scaled to match the PSD. The same process was carried out for the boxes based on the CT shapes. A spherical harmonic series was derived and used for the boxes, so that all particles used were treated equally. For the boxes, using a spherical harmonic series representation meant that the corners were rounded to some extent.¹⁹ A water:cement mass ratio (w/c) of 0.50 was used for all mixes, and all the simulations were run on the same computer, a desktop PC using Linux and running VCCTL 7.0. All the hydration simulations used isothermal conditions ($T = 23^\circ\text{C}$) and saturated curing.

Table I summarizes the set point behavior of all five systems. The second column is the degree of hydration, averaged over the five independent systems, at which 40% of the solids belonged to a percolated cluster. This point has been shown to correspond closely to initial set as indicated by the Vicat needle test.^{37,38} The actual point where the model would have a nonzero shear modulus would be at a degree of hydration slightly less than this point. The second column indicates the average degree of hydration when 95% of the solids belonged to a percolated cluster. The uncertainties quoted are ± 1 SD from the mean of five microstructures, each of which was hydrated once. The degree of hydration where 40% of the solids are part of a percolated or connected cluster show that, within the quoted uncertainties, the spheres act differently from the other particles, which all have very similar behavior. The set points are given in terms of degree of hydration, not time. If they were given in terms of time, then the smaller surface area of the spherical particles might have played a role, with a smaller early age reactivity giving a longer set time, but using degree of hydration takes out this variable. Therefore the only differences in Table I reflect differences in particle shape.

It is possible that the more prolate particles, the FIB-NT particles and boxes, need a slightly lower amount of hydration for set to occur than the X-ray CT particles and boxes (see Table I), but this difference is small and is within the uncertainty limits. In another kind of percolation problem, randomly overlapping ellipsoids of revolution required a smaller volume fraction of particles to percolate as the particles became more prolate.³⁹ In particular, it is quite clear that the boxes modeled on the real particles and the real particles themselves have nearly identical set point behavior in the two comparisons that can be made in Table I.

VI. Summary and Conclusions

For the same cement that was ground in a roller mill, the VESD size ranges of 0.4–2.0 μm and 20–60 μm were compared. 3-D

images were obtained using a dual focused ion beam technique for the smaller particles and X-ray CT for the larger particles. By using the same spherical harmonic analysis technique for both image sets, various shape parameters were computed and compared.

The clear conclusion was that although both sets of particles tended to be prolate, $\langle L \rangle > \langle W \rangle$, the smaller particles were more prolate than the larger particles, with a greater average length and a greater average length to width ratio. The average widths were much closer, so that almost all the difference in the average length to width ratio came from the greater average length of the smaller particles.

The exact reason for this difference is not known, although it probably arises from the grinding of the much larger clinker particles, since all size cement particles participate in this process. It is possible that smaller particles arise in the grinding process by being “chipped” off the surface of larger particles, which could give rise to more prolate particles. It is also possible that the added gypsum particles in the cement tend to be more easily grindable⁴⁰ and split into smaller pieces, and thus could have formed a larger mass percentage of the FIB particles. This shape difference was small but real, given the uncertainties involved in the experiments and their statistical analysis. It was noted that the values of the ratio \mathcal{I} of the maximum principal moment of inertia to the minimum principal moment of inertia tended to be higher than the ratio \mathcal{R} of the length to the width of the particles. This was because, as was demonstrated in Appendix A for an exact case, \mathcal{I} tends to be roughly proportional to the square of \mathcal{R} . One must keep this fact in mind when using only \mathcal{I} or \mathcal{R} to evaluate shape differences between particles.

One practical effect of this small but real average shape difference was seen by preparing model particles, with identical PSDs, with spherical, CT, FIB-NT, and boxes that roughly followed the FIB-NT and CT length–width statistics. The only difference between the five sets of particles was shape. It was found that spheres took a significantly larger degree of hydration to reach the set point, but the other shapes all took about the same amount of hydration, within numerical uncertainty. From this it is concluded that as model particles with the correct overall shape geometry are prepared, the exact shape will not affect the model results for set point. Therefore, perhaps one does not have to prepare model particles, at least in the size range of 0.4–60 μm , whose shape depends on size. This conclusion is based on one kind of cement, but this conclusion is expected to hold for other cements, since cement particle shape, at least for what has been investigated up to now, depends only mildly on cement chemistry.¹⁴ However, there could be other effects of particle shape at early age, including the elastic moduli, which have not been investigated in this study.

Appendix A

(A.1) Exact Calculation for a Simple Shape Distribution of the Moment of Inertia and Length:Width Ratio for Rectangular Boxes or Ellipsoids

For rectangular box-shaped particles, the exact formulas for the average value of the ratio of the largest principal moment of inertia to the smallest principal moment of inertia, denoted \mathcal{I} , and the average value of the length to width ratio, \mathcal{R} , can be calculated. The same analysis will also hold for triaxial ellipsoids.

Consider the following model particles: rectangular parallelepiped boxes of length (L), width (W), and thickness (T). Without loss of generality, define $T=1$ always (then L and W are similar to the normalized quantities defined in the paper). Since by definition, $L > W > T$, the maximum principal moment of inertia is $\alpha(L^2 + W^2)$, and the minimum principal moment of inertia is $\alpha(W^2 + T^2)$, where $\alpha = 1/3$ for boxes and $1/5$ for triaxial ellipsoids.^{21,22} Therefore \mathcal{R} and \mathcal{I} are defined as follows:

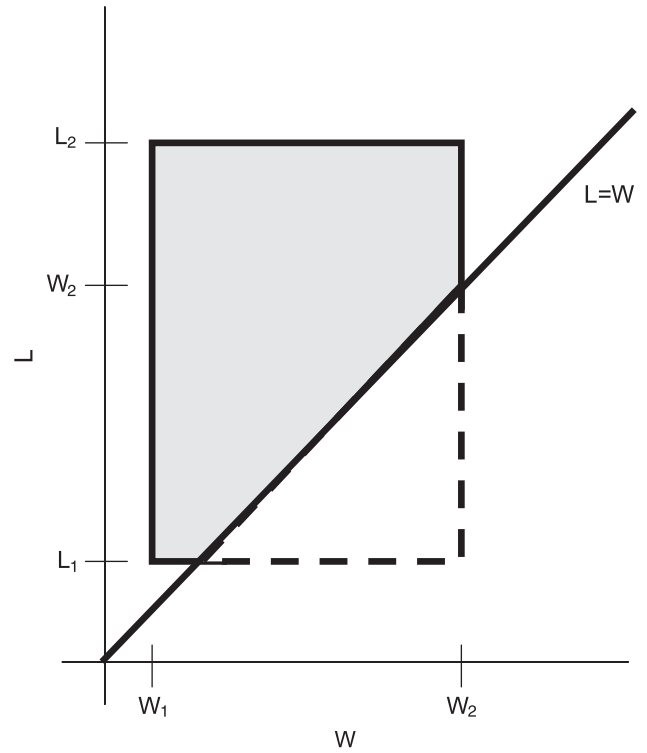


Fig. A1. The allowed region (shown in light gray) for the length (L) and width (W) of the rectangular boxes. Note that the figure is drawn for the case where $W_1 < L_1 < W_2 < L_2$. If $L_1 > W_2$, then the gray region would be entirely above the $L = W$ line and would be a simple rectangular shape.

$$\mathcal{R} = \left\langle \frac{L}{W} \right\rangle \quad \mathcal{I} = \left\langle \frac{(L^2 + W^2)}{(W^2 + 1)} \right\rangle \quad (\text{A-1})$$

Just from the structure of Eq. (A-1), one might guess that \mathcal{I} is roughly the square of \mathcal{R} .

A simple probability distribution for L and W is that pairs of (L, W) values are uniformly distributed in the region $L_1 < L < L_2$, and $W_1 < W < W_2$, subject to the requirement that $L \geq W$. The possible region, of area A and shown in gray, lies inside the solid black lines.

Based on Fig. A1 it is simple to calculate A as the area of the entire rectangle minus the area of the right triangle with a dashed outline:

$$A = (L_2 - L_1)(W_2 - W_1) - \frac{1}{2}(W_2 - L_1)^2 \quad (\text{A-2})$$

so that $P(L, W) = 1/A$ is the uniform probability distribution for this case. Note that when $W_2 = L_1$, the second term is zero as it ought to be. When $W_2 < L_1$, the second term in the area is dropped.

To do the various integrals needed to calculate \mathcal{R} and \mathcal{I} , one integrates over the complete rectangular area in Fig. A2, then subtracts the integral over the dashed right triangle. The integrals that define \mathcal{R} and \mathcal{I} are:

$$\mathcal{R} = \frac{1}{A} \int_{L_1}^{L_2} dL \int_{W_1}^{W_2} dW \frac{L}{W} - \frac{1}{A} \int_{L_1}^{W_2} dL \int_{L_1}^W dW' \frac{L}{W'} \quad (\text{A-3})$$

$$\mathcal{I} = \frac{1}{A} \int_{L_1}^{L_2} dL \int_{W_1}^{W_2} dW \frac{(L^2 + W^2)}{(W^2 + 1)} - \frac{1}{A} \int_{L_1}^{W_2} dL \int_{L_1}^W dW' \frac{(L^2 + W'^2)}{(W'^2 + 1)} \quad (\text{A-4})$$

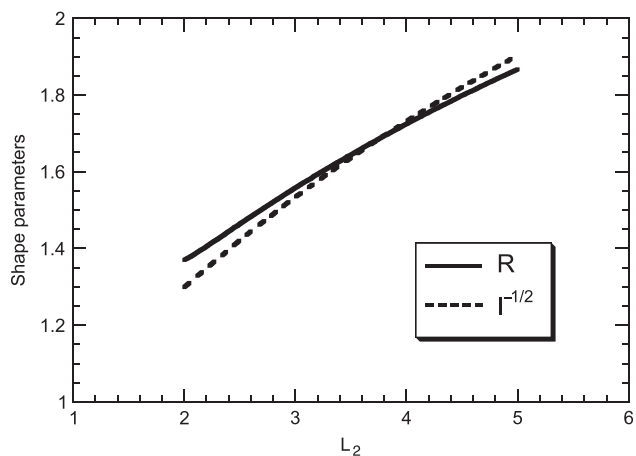


Fig. A2. The shape parameters \mathcal{R} and the square root of \mathcal{I} , where \mathcal{R} and \mathcal{I} are defined in the text, are plotted versus the value of L_2 , with $L_1 = W_1 = 1.0$ and $L_2/W_2 = 1.6$.

Equations (A-3) and (A-4) are combinations of elementary integrals but the results are fairly complicated:

$$R = \frac{1}{2A} \left[L_2^2 \ln\left(\frac{W_2}{W_1}\right) - L_1^2 \ln\left(\frac{L_1}{W_1}\right) + \frac{1}{2}(L_1^2 - W_2^2) \right] \quad (\text{A-5})$$

$$I = \frac{1}{A} \left[\begin{aligned} &L_2 \left(\frac{1}{3} L_2^2 - 1 \right) \{ \tan^{-1}(W_2) \tan^{-1}(W_1) \} + \\ &L_1 \left(\frac{1}{3} L_1^2 - 1 \right) \{ \tan^{-1}(W_1) \tan^{-1}(L_1) \} + \\ &L_2 W_2 - L_2 W_1 + L_1 W_1 - \frac{1}{3} (L_1^2 + 2W_2^2) + \\ &\frac{2}{3} \ln\left(\frac{W_2^2 + 1}{L_1^2 + 1}\right) \end{aligned} \right] \quad (\text{A-6})$$

A few numerical examples using these equations will be informative. For the first example, use the mean plus and minus the standard deviation as the upper and lower limits, respectively, of the FIB-NT and the CT numerical results. For the CT case, this means that $L_2 = 2.06$, $L_1 = 1.36$, $W_2 = 1.58$, and $W_1 = 1.12$. For this case, $\mathcal{I} = 1.7340$, $\mathcal{R} = 1.3057$, and the square root of \mathcal{I} is 1.3168, <1% different from the actual value of \mathcal{R} . In the FIB-NT case, $L_2 = 2.67$, $L_1 = 1.45$, $W_2 = 1.69$, and $W_1 = 1.15$. In this case, $\mathcal{I} = 2.9068$, $\mathcal{R} = 1.8693$, and the square root of \mathcal{I} is 1.7049, <9% away from the value of \mathcal{R} . For the second example, take the following assumptions: $L_1 = W_1 = 1.0$, $L_2/W_2 = 1.6$, and then plot \mathcal{R} and the square root of \mathcal{I} vs. L_2 in Fig. A2. If \mathcal{R} and the square root of \mathcal{I} were exactly equal, then the quadratic relationship would be exactly true. Some deviation between the two curves in Fig. A2 indicate that the relationship is only approximate, but fairly robust across a range of values of W_2 and L_2 .

Acknowledgments

We would like to thank the National Synchrotron Light Source at Brookhaven National Laboratory, which is supported by the U.S. Department of Energy, Division of Materials Sciences and Division of Chemical Sciences, under Contract No. DE-AC02-98CH10886, for hosting us to do the X-ray CT measurements. We would also like to thank Dr. K. A. Snyder for useful conversations about the statistical analysis of the two sets of particles, and Dr. Stephen Farrington of BASF Construction Chemicals, LLC for critically reading the manuscript.

References

- ¹J. F. Douglas and E. J. Garboczi, "Intrinsic Viscosity and Polarizability of Particles Having a Wide Range of Shapes," *Adv. Chem. Phys.*, **91**, 85–153 (1995).
- ²E. J. Garboczi and J. F. Douglas, "Intrinsic Conductivity of Objects Having Arbitrary Shape and Conductivity," *Phys. Rev. E*, **53**, 6169–80 (1996).

- ³M. L. Mansfield, J. F. Douglas, and E. J. Garboczi, "Intrinsic Viscosity and the Electrical Polarizability of Arbitrarily Shaped Objects," *Phys. Rev. E*, **64**, 61401–16 (2001).
- ⁴G. Polya and G. Szego, *Isoperimetric Inequalities in Mathematical Physics*. Princeton University Press, Princeton, 1951.
- ⁵ASTM Standard Test Method for Flat Particles, Elongated Particles, or Flat and Elongated Particles in Coarse Aggregate (D 4971). ASTM, West Conshohocken, PA.
- ⁶E. J. Garboczi and J. W. Bullard, "Shape Analysis of a Reference Cement," *Cem. Conc. Res.*, **34**, 1933–7 (2004).
- ⁷J. W. Bullard and E. J. Garboczi, "A Model Investigation of the Influence of Particle Shape on Portland Cement Hydration," *Cem. Conc. Res.*, **36**, 1007–15 (2006).
- ⁸N. S. Martys, "Study of a Dissipative Particle Dynamics Based Approach for Modeling Suspensions," *J. Rheol.*, **49**, 401–24 (2005).
- ⁹S. T. Erdoğan, D. W. Fowler, and E. J. Garboczi, "Shape and Size of Microfine Aggregates: X-Ray Microcomputed Tomography vs. Laser Diffraction," *Powder Technol.*, **177**, 53–63 (2007).
- ¹⁰T. Matsuyama, H. Yamamoto, and B. Scarlett, "Transformation of Diffraction Pattern Due to Ellipsoids into Equivalent Diameter Distribution for Spheres," *Part. Part. Syst. Charact.*, **17**, 41–6 (2000).
- ¹¹N. Gabas, N. Hiquily, and C. Laguérie, "Response of Laser Diffraction Particle Sizer to Anisometric Particles," *Part. Part. Syst. Charact.*, **11**, 121–6 (1994).
- ¹²H. Mühlenweg and E. D. Hirleman, "Laser Diffraction Spectroscopy: Influence of Particle Shape and a Shape Adaptation Technique," *Part. Part. Syst. Charact.*, **15** [4] 163–9 (1998).
- ¹³Z. H. Ma, H. G. Merkus, J. G. A. E. de Smet, C. Heffels, and B. Scarlett, "New Developments in Particle Characterization by Laser Diffraction: Size and Shape," *Powder Technol.*, **111**, 66–78 (2000).
- ¹⁴S. T. Erdoğan, X. Nie, P. E. Stutzman, and E. J. Garboczi, "Micrometer-Scale 3-D Shape Characterization of Eight Cements: Particle Shape and Cement Chemistry, and the Effect of Particle Shape on Laser Diffraction Particle Size Measurement," *Cem. Conc. Res.*, (2010), doi: dx.doi.org/10.1016/j.cemconres.2009.12.006.
- ¹⁵D. P. Bentz, S. Mizell, S. G. Satterfield, J. Devaney, W. George, P. M. Ketcham, J. Graham, J. Porterfield, D. Quenard, F. Vallee, H. Sallee, E. Boller, and J. Baruchel, "The Visible Cement Data Set," *J. Res. Nat. Inst. Stand. Technol.*, **107** [2] 137–48 (2002).
- ¹⁶L. Holzer, B. Muench, M. Wegmann, P. Gasser, and R. J. Flatt, "FIB-Nanotomography of Particulate Systems — Part I: Particle Shape and Topology of Interfaces," *J. Am. Ceram. Soc.*, **89**, 2577–85 (2006).
- ¹⁷B. Muench, P. Gasser, L. Holzer, and R. Flatt, "FIB-Nanotomography of Particulate Systems — Part II: Particle Recognition and Effect of Boundary Truncation," *J. Am. Ceram. Soc.*, **89**, 2586–95 (2006).
- ¹⁸L. Holzer, F. Indutnyi, P. Gasser, B. Muench, and M. Wegmann, "3D Analysis of Porous BaTiO₃ Ceramics using FIB Nanotomography," *J. Microsc.*, **216**, 84–95 (2004).
- ¹⁹E. J. Garboczi, "Three-Dimensional Mathematical Analysis of Particle Shape Using X-Ray Tomography and Spherical Harmonics: Application to Aggregates Used in Concrete," *Cem. Conc. Res.*, **32**, 1621–38 (2002).
- ²⁰M. A. Taylor, E. J. Garboczi, S. T. Erdoğan, and D. W. Fowler, "Some Properties of Irregular Particles in 3-D," *Powder Technol.*, **162**, 1–15 (2006).
- ²¹J. W. Bullard, C. F. Ferraris, E. J. Garboczi, N. S. Martys, and P. A. Stutzman, "Virtual Cement and Concrete"; pp. 1311–31 in *Innovations in Portland Cement Manufacturing, Chapter 10.3*, Edited by J. I. Bhatti, F. M. Miller, and S. H. Kosmatka. Portland Cement Association, Portland, 2004.
- ²²D. P. Bentz, E. J. Garboczi, J. W. Bullard, C. F. Ferraris, and N. S. Martys, "Virtual Testing of Cement and Concrete"; pp. 38–50 in *Significance of Tests and Properties of Concrete and Concrete-Making Materials, ASTM STP 169D*, Edited by Lamond J., and Pielert J., ASTM International, West Conshohocken, PA, 2006.
- ²³J. W. Bullard, "A Three-Dimensional Microstructural Model of Reactions and Transport in Aqueous Mineral Systems," *Mod. Simul. Mater. Sci. Eng.*, **15**, 711–38 (2007).
- ²⁴J. W. Bullard, "A Determination of Hydration Mechanisms for Tricalcium Silicate Using a Kinetic Cellular Automaton Model," *J. Am. Ceram. Soc.*, **91**, 2088–97 (2008).
- ²⁵A. C. Kak and M. Slaney, *Principles of Computerized Tomographic Imaging*. SIAM, New York, 2001.
- ²⁶E. J. Garboczi, G. S. Cheok, and W. C. Stone, "Using LADAR to Characterize the 3-D Shape of Aggregates: Preliminary Results," *Cem. Conc. Res.*, **36**, 1072–5 (2006).
- ²⁷M. Grigoriu, E. J. Garboczi, and C. Kafali, "Spherical Harmonic-Based Random Fields for Aggregates Used in Concrete," *Powder Technol.*, **166**, 123–38 (2006).
- ²⁸S. T. Erdoğan, P. N. Quiroga, D. W. Fowler, H. A. Saleh, R. A. Livingston, E. J. Garboczi, P. M. Ketcham, J. G. Hagedorn, and S. G. Satterfield, "Three-Dimensional Shape Analysis of Coarse Aggregates: New Techniques for and Preliminary Results on Several Different Coarse Aggregates and Reference Rocks," *Cem. Conc. Res.*, **36**, 1619–27 (2006).
- ²⁹G. Arfken, *Mathematical Methods for Physicists*. Academic Press, New York, 1970.
- ³⁰G. W. Snedecor and W. G. Cochran, *Statistical Methods*, 7th edition, The Iowa State University Press, Ames, IA, 1980.
- ³¹H. Goldstein, C. P. Poole, and J. L. Safko, *Classical Mechanics*. Addison Wesley, New York, 2002.
- ³²D. P. Bentz, "Three-Dimensional Computer Simulation of Portland Cement Hydration and Microstructure Development," *J. Am. Ceram. Soc.*, **80**, 3–21 (1997).
- ³³E. J. Garboczi and D. P. Bentz, "The Effect of Statistical Fluctuation, Finite Size Error, and Digital Resolution on the Phase Percolation and Transport

Aspects of the NIST Cement Hydration Model," *Cem. Conc. Res.*, **31**, 1501–14 (2001).

³⁴D. P. Bentz, E. J. Garboczi, C. J. Haecker, and O. M. Jensen, "Effects of Cement Particles Size Distribution on Performance Properties of Portland Cement-Based Materials," *Cem. Conc. Res.*, **29**, 1663–71 (1999).

³⁵A. P. Roberts and E. J. Garboczi, "Computation of the Linear Elastic Properties of Random Porous Materials with a Wide Variety of Microstructure," *Proc. Roy. Soc. Lond. A*, **458**, 1033–54 (2002).

³⁶A. P. Roberts and E. J. Garboczi, "Elastic Properties of Model Porous Ceramics," *J. Am. Ceram. Soc.*, **83**, 3041–8 (2000).

³⁷D. P. Bentz, "Cement Hydration: Building Bridges and Dams at the Microstructure Level," *Mater. Struct.*, **40**, 397–404 (2007).

³⁸G. Sant, M. Dehadrai, D. P. Bentz, P. Lura, C. F. Ferraris, J. W. Bullard, and J. Weiss, "Detecting the Fluid-to-Solid Transition in Cement Pastes," *Concr. Int.*, **31**, 53–8 (2009).

³⁹E. J. Garboczi, K. A. Snyder, J. F. Douglas, and M. F. Thorpe, "Geometrical Percolation Threshold of Overlapping Ellipsoids," *Phys. Rev. E*, **52**, 819–28 (1995).

⁴⁰L. M. Hills, "The Effect of Clinker Microstructure on Grindability: Literature Review Database"; PCA Report 331, 1995. □